Numerical study of the dynamic response of a wind turbine on a tension leg platform with a coupled partitioned six degree-of-freedom rigid body motion solver

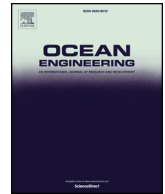Chow, Jeng Hei; Srikanth, Narasimalu; Ng, Eddie Yin Kwee

2018

Numerical study of the dynamic response of a wind turbine on a tension leg platform with a coupled partitioned six degree-of-freedom rigid body motion solver

Jeng Hei Chow[a,*], Eddie Y.K. Ng[a], Narasimalu Srikanth[b]

[a] School of Mechanical and Aerospace Engineering, Nanyang Technological University, Singapore
[b] Renewables & Low Carbon Generation (Wind & Marine), Energy Research Institute @ NTU (ERI@N), Singapore

ABSTRACT

In assessment of the response of floating wind turbines under extreme wave conditions, structure stability and survivability is of utmost importance in the design and implementation. The experimental upwind horizontal axis floating wind turbine on a tension leg platform (TLP) setup was validated with the strongly coupled partitioned six degree-of-freedom rigid body motion solver (Chow and Ng 2016). After tuning of the unknown variables such as the tendon stiffness and damping coefficients with the decay tests, the system ran with the coupled fluid-motion numerical solver resulted in accurate estimations of the natural frequencies and damping ratios. Together with a modified restrain system to model the tendons, the response of the floating wind turbine under regular and focused waves simulations were found to be well-predicted. A stability analysis was performed to determine the iterations that should be ran every time step. The median of the time steps converged within 8.7 iterations.

1. Introduction

Over the years, the wind power industry has witnessed the transition from fixed to floating foundations. With the increasing demand for higher capacity generators, there is a trend for wind turbines in general to be situated further offshore with the prevalence of stronger winds (Roland Berger, 2013). Shifting further offshore brings along challenges to develop structures with higher stiffness to withstand the environmental loads. This becomes more apparent as the natural frequency of the fixed structure approaches the wave frequencies, resulting in a drop in cost-effectiveness beyond a depth of 60 m (Butterfield et al., 2006). It is thus not surprising for the industry to focus the research on floating foundations for wind turbines. Based on studies on the levelised cost of energy (LCOE) of different types of offshore floating wind turbines, it can be expected that for deeper waters corresponding to about 100 km offshore, the increase in LCOE is lesser than their fixed foundation counterparts (Myhr et al., 2014).

It is clear that the major challenges lie in the design and safety assessments in the construction of such structures. Other than experimental tests, it is always useful to have a validated numerical tool to extend to the cases that are too expensive to run physical experiments on. In recent years, with improved scaling and reduced cost of

computational power, numerical analysis of floating structures has gained popularity. In order to achieve a safe but cost effective foundation for offshore floating wind turbines, it is important to have a model that can predict wave loads and responses under overturning waves, splash and extreme run-up. Other common phenomena such as water-on-deck and slamming are problems faced by the implementations as well. While highly computationally demanding, a fully non-linear Navier-Stokes (N-S) solver is often required in order to resolve the flow solution in detail. Current N-S based coupled fluid-motion solver described in Chow and Ng (2016) ensures stability of the stiff Fluid Structure Interaction (FSI) problem and yet optimises the rate of convergence.

The analysis in this study focuses on wave-structure interactions and omits the effects of the wind which can include wind-wave, wind-structure or wind-wave-structure interactions. The scope of the study lies on the response of the floating wind turbine restrained by tendons, which includes decay tests and rigid body motion under different wave conditions.

2. Experimental setup

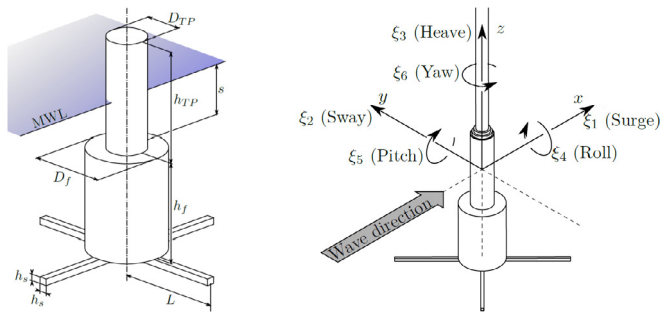The experimental prototype by Laugesen and Hansen (2015) is a

---

Fig. 1. TLP geometric parameters and submergence relative to the mean water level (MWL) (left) and global coordinate system of axes and modes (right) (Laugesen and Hansen, 2015).

Fig. 2. Clipped mesh of the full domain (left) and volume of the floating foundation (right).

TLP-restrained 1/60 Froude-scaled 10 MW floating wind turbine mounted on geometrically simple foundations shown in Fig. 1. The floating foundation is made up of a partially-submerged cylindrical transition piece (*TP*) 150 mm in diameter and 533 mm in height at the top supporting the rotor. The submergence of the transition piece is 200 mm. The transition piece is supported by a floater (*f*) 300 mm in diameter and 417 mm in height for additional buoyancy. Attached to the floater are slender spokes (*s*) 535 mm in length with attachment points that connect to the bottom of the wave basin by Kevlar ropes. The full model with four spokes has a total mass of 18.54 kg with a vertical centre of gravity located 321 mm above the mean water level (MWL) at $z = 0$. The mass moments of inertia I_{xx} and I_{yy} are 22.70 kgm².

The scaled wave climate or "sea states" used in the experiments were based on measurements of significant wave heights and peak periods fitted to 26 years of measurements in the Northern North Sea (Johannessen et al., 2002). 10 different environmental conditions (ECs) were selected with their wave heights H_s and peak periods T_p based on past similar experiments, with the maximum corresponding to a 50-year sea state. The wave heights and periods of the generated regular waves used in the experiments were based on the significant wave heights and peak periods for the corresponding environmental conditions. The waves were generated by a custom software input file which controls the single degree of freedom motion of the paddles. The raw experimental data recorded from the system were expected to include high frequency components that do not necessarily describe the physics based on the scale of the experiments. This was more evident in the milder sea states, relating to the lower numbered environmental conditions. In such cases a lowpass Butterworth infinite impulse response (IIR) filter was applied to the data when compared to the simulations. The highcut frequency of 20 Hz, expected to be well balanced between smoothing out the noises and still allow capturing of the higher order motion response of the system, was filtered in the forward and reverse direction to eliminate any phase distortion.

3. Simulation setup

3.1. Geometry and mesh creation

Since the study only focus on the rigid body motion of the floating wind turbine, the geometry recreated from the experiment can be simplified by omitting the model above the transition piece. A rectangular domain was formed 7 m in length, 3 m in width and 4 m in height. The horizontal coordinates of the geometric centre and/or centre of gravity of the floater was located at (0, 0) for the convenience of the six degree-of-freedom motion tracking in the analysis. The model of the floating foundation consisting of two connected cylinders, were removed from the volume of the domain (Fig. 2). The spokes of the floating foundation were omitted due to the large differences in the length scales which would require highly refined cells surrounding the
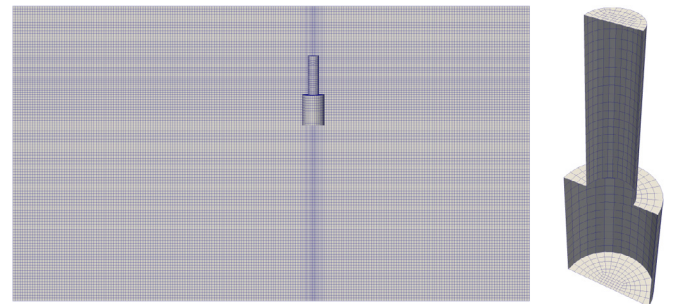
area.

For the simple geometry, a structured mesh is preferred. The vertices were joined with straight lines or circular arcs on the curved surfaces with specification of an additional interpolation point. The zones are then divided into blocks of almost the same cell size with careful calculations. A cell grading ratio of 3/2 (or 2/3) was used for the cells very close towards the foundation walls to allow sufficient resolution in the region of interest. The final mesh before any further refinement consists of around 6.69 million hexahedra cells. The cells have a maximum aspect ratio of 5.77 and a maximum skewness of 0.581. The mesh was also found to be refined enough having undergone through mesh dependence studies to ensure convergence with further refinements.

3.2. Boundary conditions

The Volume of Fluid (VoF) solver is used, where the Multidimensional Universal Limiter with Explicit Solution (MULES) algebraic scheme is employed for the advection of a sharp interface (Deshpande et al., 2012). The faces, made of four vertices each, were grouped together to form the boundaries: *west, east, south, north, bottom, top* and *body*. The *west* boundary represents the wave generator and the east boundary represents the active wave absorption mechanism. Active wave absorption (Higuera et al. 2013a, 2013b) boundary condition implemented in *ihFoam* reduces the reflection of waves by applying the correct boundary condition in the form of a velocity profile approaching the outlet boundary. The absorption system dynamically takes inputs from the measured feedback and modifies the wave-maker movements pre-emptively to eliminate the reflection of waves. For the decay tests, the wave generator and absorption boundaries were represented by no-slip walls like the rest of the concrete walls in the wave basin. Similarly, the phase fraction was set to take information from the wave generator only when wave generation was required, and set to zero gradient otherwise. No-slip walls were used for the other stationary walls and moving walls of the floating body. A special built-in boundary condition was used for the *top* patch which represents the "*atmosphere*" by switching between velocity and pressure between a constant specified value and zero gradient depending on the velocity directions. The fixed atmospheric pressure was first manually specified. For the case of inflow of air into the domain, the velocity was obtained from the normal component of the patch face. A zero gradient condition will be specified when air flows out of the domain. A fixed flux pressure analogous to buoyant pressure is specified for all the other walls except the *top* patch. The k-epsilon turbulence closure with wall functions was used in the walls for most of the cases except for some decay tests where laminar flow was required. Note that the k-omega turbulence model might be a better option due to its reputation in better resolving wake region and flow separation. However, in this case there is a need to resolve wave generation, wave absorption, and the domain as well. It is well understood that the generation and absorption model developed by IHFoam works very well with the k-epsilon model. A further

Table 1
Boundary conditions of the cases of decay tests/response under waves.

	alpha	U	p_rgh	nut	k	epsilon	pointDisplacement
west	zeroGrad/IHwaveGen	fixedValue/IHwaveGen	fixedFluxPressure	nutkWallFunc	kqRWallFunc	epsilonWallFunc	fixedValue
east	zeroGrad	fixedValue/IHwaveAbs	fixedFluxPressure	nutkWallFunc	kqRWallFunc	epsilonWallFunc	fixedValue
south	zeroGrad	fixedValue	fixedFluxPressure	nutkWallFunc	kqRWallFunc	epsilonWallFunc	fixedValue
north	zeroGrad	fixedValue	fixedFluxPressure	nutkWallFunc	kqRWallFunc	epsilonWallFunc	fixedValue
bottom	zeroGrad	fixedValue	fixedFluxPressure	nutkWallFunc	kqRWallFunc	epsilonWallFunc	fixedValue
top	inOut	pressureInOutVel	totalPressure	calculated	inOut	inOut	fixedValue
body	zeroGrad	movingWallVel	fixedFluxPressure	nutkWallFunc	kqRWallFunc	epsilonWallFunc	calculated

investigation can be done separately to look at the near field around the the structures with k-omega SST models, and perhaps look into a hybrid model. Here, we did not encouter issues with high unstable values for the k and epilon and eddy viscosity values in the flow field and at the air-water interface. The boundary conditions of this test setup are shown in Table 1.

3.3. Solver properties

The motion solver used in the simulations was based on the six DoF rigid body motion solver formulated in Chow and Ng (2016). m and I refers to the mass and moment of inertia of the floating body in kg and kg·m^2 respectively.

$$\vec{F}_{ext} + m\vec{g} + \int_S (-p\vec{n} + \vec{\tau})dS = \vec{f} \quad \vec{M}_{ext} + \int_S \vec{r} \times (-p\vec{n} + \vec{\tau})dS$$
$$= I\vec{\omega} + \vec{\omega} \times I\vec{\omega}$$

The mesh was set to move only in the regions between 0.25 m and 0.5 m away from the surface of the floating body. These values were estimated to prevent over-skewed cells too close to the boundaries and around the floating body. Based on the experimental setup, the centre of mass was set at the origin horizontally and 3.321 m from the bottom wall of the domain. The mass of the structure was set to 18.54 kg as measured in the experiments. The moments of inertia I_{xx} and I_{yy} were determined in the experiments (Laugesen and Hansen, 2015).

Based on the lengths of the spokes, the positions of the anchor and attachment points shown in Fig. 3 were determined with trigonometry. To correctly represent the four connected tendons, the simulations utilised the custom non-linear variable stiffness model. In the experiments, the tendon stiffness was tested by subjecting the tendon to known masses with increments and measuring the elongation. The loading and unloading axial strains were found to be different from each other, signifying a deviation from Hooke's law. It was decided to determine the modulus with a linear fit to the loading and unloading plots, with the y-intercept moved to zero. The *EA* value of the model was estimated to be around 80000 N, which corresponds to a fixed stiffness k of 35556 N/m taking into account the length of the tendons. This value was used in the analysis in WAMIT® but was concluded to be way over-predicted in Laugesen and Hansen (2015). A value of 6667 N/m was proposed in their study which allowed better fit of the experimental tests (Fig. 4).

The rest lengths of the tendons were estimated based on hydrostatic force conservation laws. The weight of the floating body was deducted from the buoyancy calculated from the submerged volume, resulting in the total tension of the four tendons. Depending on the stiffness, the rest length x_r can be obtained (Eq. (1)). The number of tendons, n and distance between the anchor and attachment point, x_d are known constants here with values of 4 and 2.2500 respectively. The calculated rest lengths are 2.2490 m for the tendon stiffness of 35556 N/m and 2.2447 m for 6667 N/m.

$$\rho g V - mg = nk(x_d - x_r) \tag{1}$$

The restrain system in the motion solver was also modified to take into account the Δx of the tendons falling below zero. The modification

also allows for variable stiffness, by a custom input file of the force-Δx relationship. Traditionally when modelling the restrains as linear springs, the force of the tendons acting on the floating body will fall below zero. This might be negligible in the motion of the floating body under wave loads where the tendons are usually in tension, but could affect the results for some of the modes in the decay tests. The modification here sets the force to be zero whenever Δx is negative. At every iteration the motion is solved, Δx is obtained from the subtracting the rest length from the change in position of the attachment and the anchor point. Δx is used to lookup the corresponding force from the custom input file, and multiplying the force with a unit vector pointing from the attachment to the anchor point. Additionally, the tendons have some damping property independent of the viscous damping of the floating body, which is not always easy to estimate and requires tuning from the decay tests.

The acceleration relaxation factor was set to 0.5 for the first time step, and allowed to vary from 0.1 to 1.0 for the subsequent steps based on Aitken's dynamic under-relaxation. The coupled solver controlled by the main fluid solver ran with a time step size of 10^{-4} subjected to vary based on the Courant controls. The maximum Courant numbers and maximum time step size were both capped at 0.1.
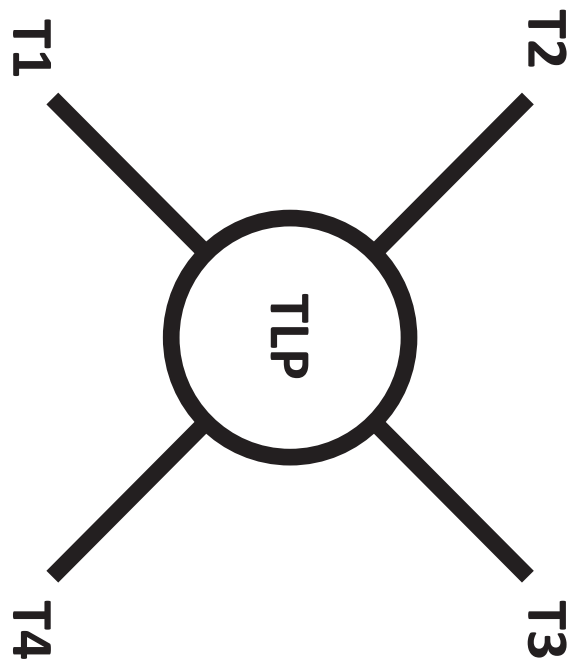
3.4. Decay tests

Model decay tests were performed in the experiments (Laugesen and Hansen, 2015) to determine the natural frequencies and damping ratios of the system. A small displacement corresponding to each degree-of-freedom was introduced and the displacements or rotations of the floating system were plotted against time. An intuitive method to obtain the natural frequencies would be to simply determine the time periods between the peaks and taking the inverse. For the damping ratios, the logarithmic decrement between subsequent peaks defined by Eq. (2) was first obtained over the first few peaks. The mean of the logarithmic decrement was used to determine the damping ratio ζ shown in Eq. (3) (Inman, 2009).

$$\delta = \ln \frac{x_i}{x_{i+1}} \tag{2}$$

$$\zeta = \frac{\overline{\delta}}{\sqrt{4\pi^2 + \overline{\delta}^2}} \tag{3}$$

For each of the modes a certain displacement was applied to the floating body and it was left to move freely. In the experiments a fishing line was attached to the location of the centre of gravity to displace it 0.11 m in the x-direction for the surge mode. In the simulations, the displacement can be easily represented by moving the anchor points by the same distance instead. For the pitch, the floating body was rotated by applying forces at the top and bottom ends in different directions. The floating body was rotated to an orientation approximately 1–1.5° from equilibrium. The forces were released simultaneously and the floating body was left to move freely. In the simulations, the exact same initial displacement method was applied here, where additional restrains were applied at the top and bottom of the floating body for the first 2 s of the simulations until it is at the correct orientation. The
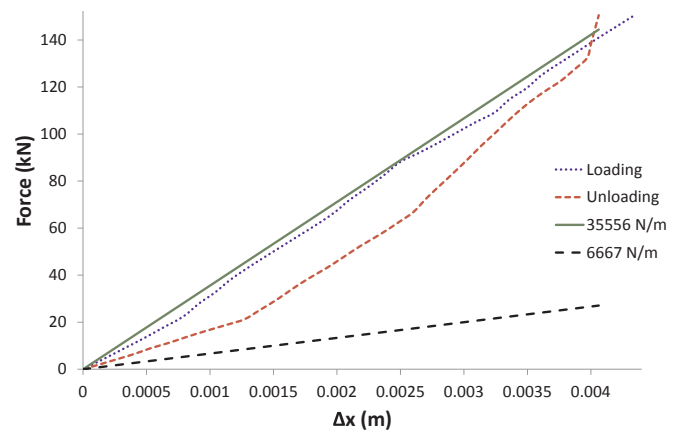
Wave generator

Fig. 4. Force elongation plots obtained during experiments and constants tested for the simulations.

be obtained. The damped natural frequency from the simulation was relatively easy to obtain and was found to be very close to the experimental value of 0.19 Hz, for the cases of different stiffness tested. Based on the methods described in the main section, a damping ratio to represent each of the response can be used as comparison (Fig. 5). In the plot, all the cases were assumed to start from an initial displacement of exactly 0.11 m as done in the experiments and follow an exponential decay trend thereafter. A constant stiffness of 6667 N/m was used. The results from the simulations showed a decent match with the experiments as long as turbulence was turned off in the fluid solver.

The damping coefficient of the tendons did not have a significant effect on the decay curve such that the value could be tuned with this mode. From the experiments, it was found that the damping of the system is one of the most difficult parameter to estimate, and thus damping ratios were assumed accurate to only one significant digit. In such case there would be no significant differences in damping ratios between the cases when different damping coefficients were used. In this test, the default 'laminar' flow did not include any damping (0 N s/m) in the tendons and the 'laminar damped' run used a fixed damping coefficient of 35 N s/m in Fig. 5. In the simulation cases where the geometry only consists of the floater, the sway is expected and assumed to have the same natural frequency and damping ratios as the surge mode.

3.4.2. Yaw

The yaw motion was expected to be dependent on the moment of inertia of the vertical axis I_{zz} which was unfortunately not measured in

TLP

Active wave absorption

Fig. 3. Layout of spokes and tendon attachment point locations (Not drawn to scale).

restrains were released thereafter, continuing on with the simulation. The yaw decay tests were performed in a similar manner in the experiments. Forces were applied at opposite ends to rotate the floating body in the z-axis by approximately 10–15°.

3.4.1. Surge

From the surge response, the periods and decrements of peaks can
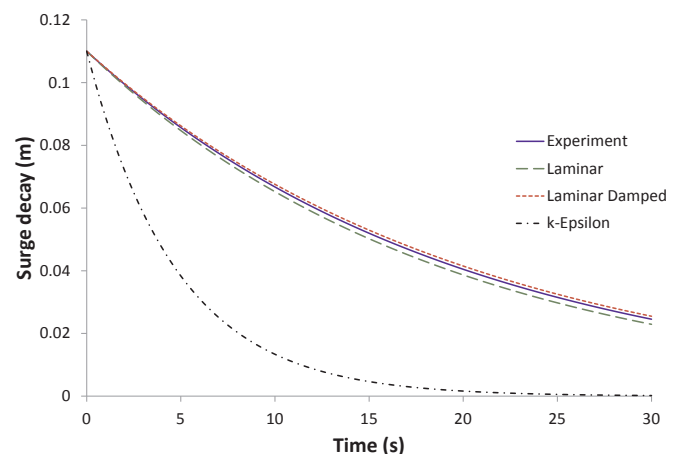

Fig. 5. Decay of the surge mode between experiments and different simulation settings.

the experiments (Laugesen and Hansen, 2015). From several tests, it was found that the natural frequency varies with different values of I_{zz}, and a value of 1.1 kg m^2 corresponds to the natural frequency of exactly 0.63 Hz. On the other hand, the damping ratio was found to be un-affected by any of the other unknown variables. The damping ratio obtained in the simulations was way under-predicted. One possible reason for the low damping ratio was thought to be due to the absence of spokes in the geometry which could have contributed to significant damping in the yaw decay, despite being slender. To test the hypothesis by including the spokes in the geometry, a huge refinement in mesh would be required around the spokes. The hypothesis was thus untested in this study.

3.4.3. Pitch

The pitch motion was the most difficult to perform decay test experiments on, due to the short period of times where the floating body was unrestrained and free-floating during the rotation decay. In the simulations of this study, unrestrained floating bodies are more prone to instabilities and would thus require a much reduced Courant number and time step size for convergence. Adding to that, the lack of knowledge of the damping coefficient in the tendons would mean that some sort of trial and error and tuning was required. From the simulated response of the pitch, it can be confirmed that using the measured stiffness of 35556 N/m resulted in an over-predicted natural frequency of 4.4 Hz. As expected when a reduced stiffness of 6667 N/m was used for the simulated decay tests, a frequency of 2.0 Hz was obtained, much closer to the experimental results of 1.9 Hz. The natural frequency varied slightly, between 1.8 Hz and 2.0 Hz when different damping coefficients were used for the tendons, but the differences were also not large enough for tuning.

The damping ratio, on the other hand increased almost linearly with the damping coefficient of the tendons, which allowed for easy tuning of the parameter. Based on the plots of damping ratio vs the damping coefficients (Fig. 6), it was found that the experimental damping ratio of 0.04 would require a tendon damping coefficient of around 35 N s/m for a stiffness of 6667 N/m and 33 N s/m for a stiffness of 35556 N/m based on linear correlations. On another plot of the decay curves (Fig. 7), it can be observed that a better fit was obtained with a damping coefficient of 25 N s/m. This was attributed to the slight over-prediction in the natural frequency of 2.0 Hz since the constant decay rate used in the plots consist of both the damping ratio and the damped natural frequency. The differences between the two damping coefficients would however result in insignificant deviations when the damping ratio is compared to the experiments, and no differences when rounded to one significant figure.
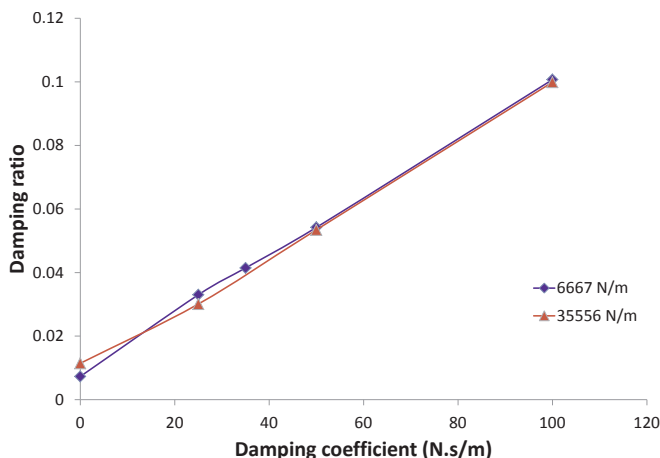

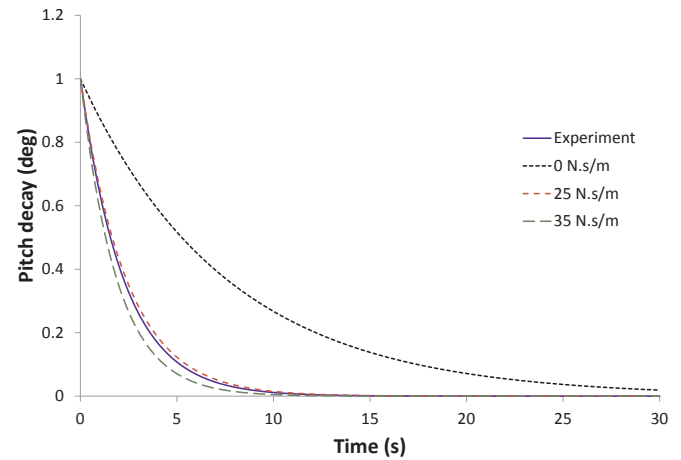**Fig. 6.** Plot of damping ratio vs damping coefficient in the tendons.

Fig. 7. Decay of the pitch mode between experiments and different rope damping.

3.4.4. Finalised parameters

Most of the natural frequencies and damping ratios matched the experimental values with the exception of the damping ratio in the yaw mode. Some of the unknown parameters have been tuned in the tests based on the experimental results. The reduced stiffness of 6667 N/m was deemed to be more correct due to the natural frequency obtained in the pitch. The moment of inertial I_{zz} was set to 1.1 kg m^2 to obtain the experimental natural frequency in the yaw mode. The pitch response provided with sufficient information to determine the damping in the tendons to be 35 N s/m. In the next section, these finalised parameters were fed into the solver for subsequent simulations in the response of the floating structure under wave loads.

3.5. Floating structure under regular waves

The response of the floating structure under wave loads, in a coupled Navier-Stokes based solver requires a functioning dynamic wave generation/absorption boundary condition. The *ihFoam* wave generation and absorption boundary conditions (Higuera et al. 2013a, 2013b) were used in the setup on the west and east boundaries respectively to replace the no-slip walls in the decay tests. In general, it was expected for more severe wave conditions in experiments to have a better fit with simulated data due to the larger wave periods and wave heights. It was thus decided to compare the response of the structure under regular waves based on the wave periods and heights of EC08 (H_s = 0.167 m, T_p = 1.58 s) and EC10 (H_s = 0.239 m, T_p = 1.99 s). The simulations were ran for 20 s under the generated waves which would provide sufficient results for comparisons both in the time and frequency domain. The simulations were ran by the new Intel$^®$ Xeon$^®$ processor 5500 series 32 cores at NTU HPC. The simulations took 28.5 h to complete.

In the comparison with the experiments, a certain time lag was introduced to the experimental values to match the steady, regular peaks and troughs. For the six degree-of-freedom responses of the floating structure, the mean of the simulated response were deducted from the experimental response, to take into account the small differences in the zero level.

3.5.1. Motion response

The translational modes of interest for uni-directional wave loads of heading θ = 0° would be the surge and the heave, with the sway at an insignificant magnitude. From the industrial viewpoint, the surge response of the floating wind turbine is of utmost importance in the design parameterisation of the tendons' stiffness, rest length and maximum surge displacement under a certain wave load. The heave, on the other hand is expected to be small and usually damped and thus less of a concern. Using the tuned parameters in the decay tests, it was found
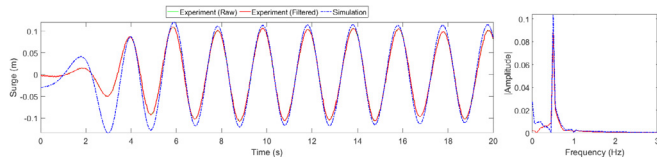
Fig. 8. Surge response under regular waves of EC10, $\theta = 0°$.
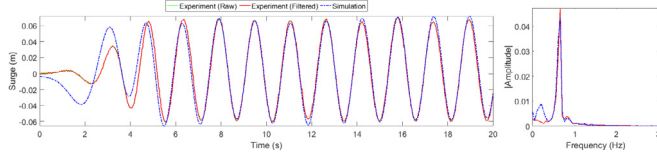
Fig. 9. Surge response under regular waves of EC08, $\theta = 0°$.

that the surge response in the simulations matched the experimental results very well once a steady response was obtained (Fig. 8). From the Fast-Fourier Transform (FFT) analysis of the first 20 s, it can be seen that the main wave frequency near 0.5 Hz was obtained, which corresponds to the generated waves with a period of 1.99 s. The findings were evident in the sea-states with greater wave heights and periods such as EC8 and EC10 (Figs. 8 and 9).

A case was ran with generated regular waves of 30° heading to show the significant amount of sway response of the floating structure. For simplicity, the floating system in the simulation was rotated 30° clockwise to mimic a counter-clockwise domain rotation as seen in Fig. 10. Physically, only the anchor and attachment points were rotated with the origin at the centre of the floating wind turbine. The six degree-of-freedom responses obtained were mapped back into the original orientation. From Fig. 11, it was found that both the surge and sway simulated responses fit the measurements very well after 10 s of

Fig. 10. Layout of spokes and tendon attachment point locations (Not drawn to scale).
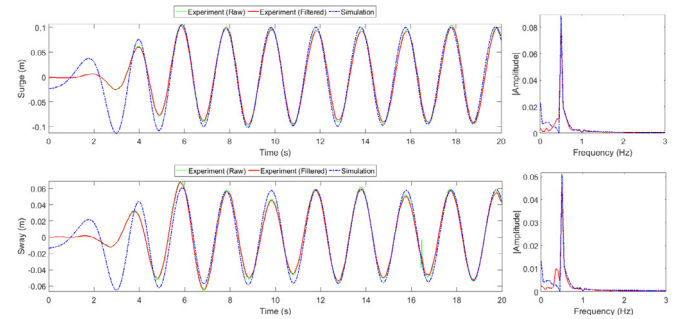
Fig. 11. Surge and sway response under regular waves of EC10, $\theta = 30°$.

simulation as the directional waves approaches steady state. A main wave frequency of 0.5 Hz was obtained in the frequency plots as well.

The simulated heave responses were expected to not fit the experimental results as well as surge due to the much smaller magnitude. The heave mode is also has more noise before the start of the simulation when there are no loads. The results were surprisingly satisfactory in such a highly dynamic case where the FFT plots showed that the both the peaks at 0.5 Hz and about 1.25 Hz were captured. In wave condition EC10 (Fig. 12), the amplitude of the peak at 0.5 Hz was found to be under-predicted, which was not evident in EC08 (Fig. 13) where a much better fit was observed for both major frequencies. It is interesting to note that despite having a noisier measured data for EC08, the simulation produced a better match capturing more of the lower frequency peak at 0.5 Hz. In a similar manner for the responses under regular waves of 30° heading (Fig. 14), the double peaks in the measured and simulated data were prominent just like the cases with generated waves of 0° heading. The results are comparable to the case of the same sea state of EC10, but not as good as EC08.

The rotational mode yaw is negligible in the cases here and not compared with the experiments. Simulation results of the pitch mode compared decently well with the measurements for both EC08 and EC10 under zero heading (Figs. 15 and 16). In the FFT plots for the cases, the peaks were located at 0.5 Hz which corresponds to the generated wave period of 1.99 s. The peaks were slightly under-predicted from the measurements for both cases. The pitch and roll responses for the generated regular waves of 30° heading were determined as well (Fig. 17). The simulated pitch response similarly matched with the measurements, with slightly under-predicted peaks and troughs. The experimental roll responses were found to be more susceptible to some fluctuations occurring at around 1 Hz which was not picked up in the solver.

3.5.2. Forces on the restrains

Other than the six degree of freedom response of the floating structure, the parameterisation in design lies on the rest length and material stiffness required for the tendons connecting the wind turbine to the bottom of the wave basin. From the tests, the range of tension experienced by the tendons under different wave conditions will be vital. Note that the time lag introduced in this case were the same as the value introduced in the surge and heave responses to fit the experimental and simulated curves. From the comparisons of the experimental and simulated tension, some slight discrepancies were detected (Figs. 18 and 19).
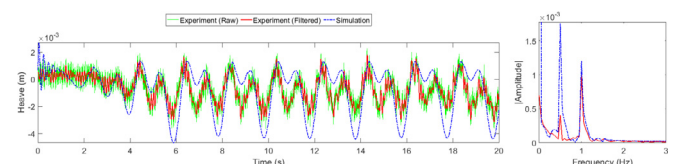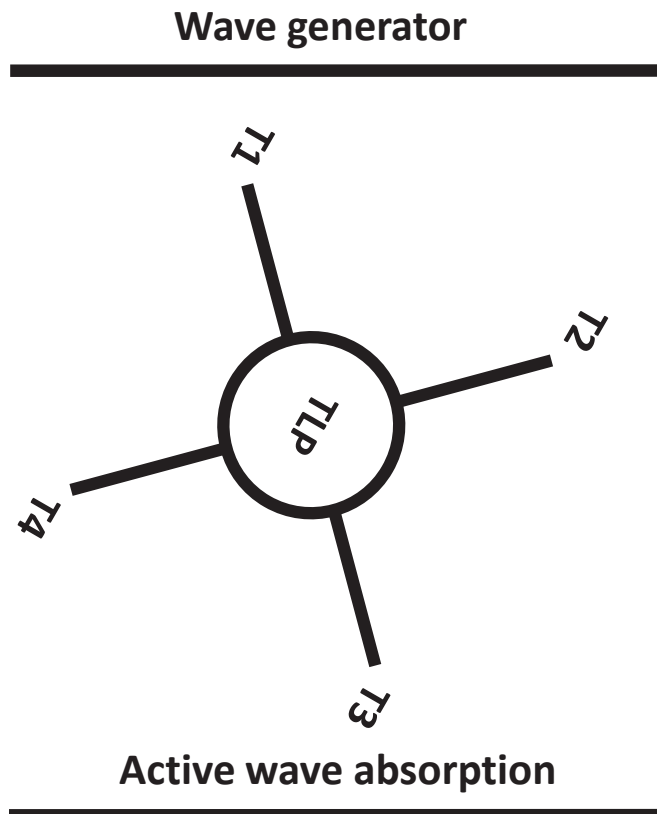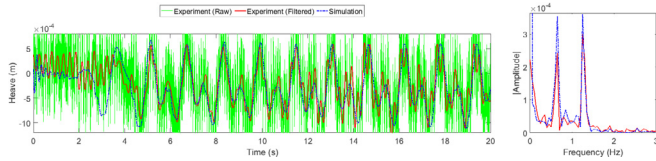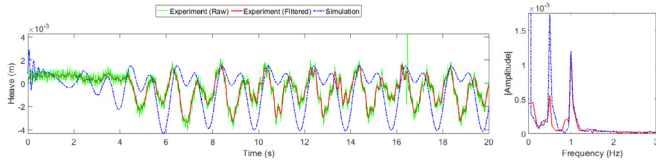

Fig. 12. Heave response under regular waves of EC10, $\theta = 0°$.

Fig. 13. Heave response under regular waves of EC08, $\theta = 0°$.

Fig. 14. Heave response under regular waves of EC10, $\theta = 30°$.
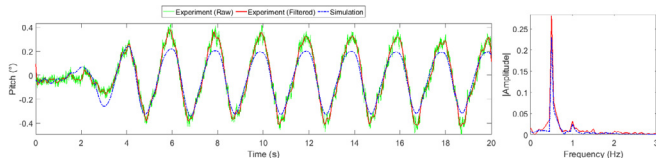
Fig. 15. Pitch response under regular waves of EC10, $\theta = 0°$.
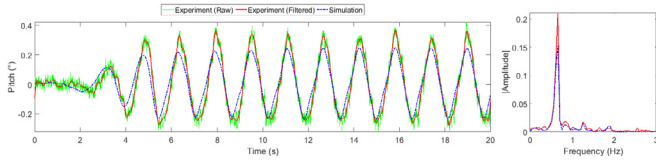
Fig. 16. Pitch response under regular waves of EC08, $\theta = 0°$.
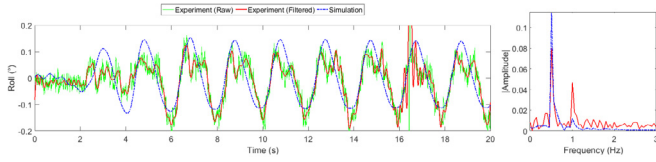
Fig. 17. Roll and pitch response under regular waves of EC10, $\theta = 30°$.
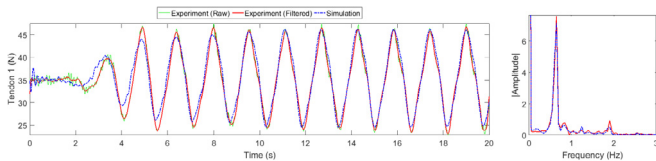
Fig. 18. Tension of upstream tendons under regular waves of EC08, $\theta = 0°$.

The results showed small differences in the maximum and minimum values between the upstream tendons 1 and 2, and also between the downstream tendons 3 and 4. From Fig. 18, there are clear differences
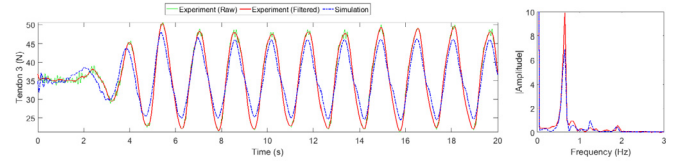
Fig. 19. Tension of downstream tendons under regular waves of EC08, $\theta = 0°$.

between the experimental measured tensions between the two upstream tendons, unlike the simulated results showing consistency in symmetry. It is unclear with the available results the reason for the differences. One possibility would be the additional tendon length between the anchor points and the control points which may have affected the recorded tensions in the z-gauges. The z-gauges weigh about 250 g each and could have an effect on the measurements too. The tension of the downstream tendons has fewer errors in measurements between the tendons (Fig. 19), and thus produced a better fit with the simulated data.

3.5.3. Solver stability

The strongly coupled motion solver with Aitken's dynamic under-relaxation was designed to ensure stability in the iterations leading to the end of the time step once the motion solution converges. Stability is achieved by the solver dynamically reducing the weightage of the calculated acceleration in the new iteration with Aitken's under-relaxation. However, it was discovered from the simulations that if the fluid solver did not have a sufficiently small time step size, several time steps may struggle with motion convergence, reaching the maximum stipulated iterations per time step of 100 with relative errors still larger than 10^{-3}. It was realised that when the Courant numbers controlling the fluid solver time steps were reduced, the relative errors in the motion solver decreased faster and thus achieved convergence within lesser number of iterations. This is of course under the assumption that the fluid solver achieved convergence before the motion solver. This phenomenon is not surprising and is a direct consequence of the decoupled time step controls in the fluid and motion solvers. In most dynamic runs, a Courant number of 0.1 would be sufficiently small to ensure the motion do not face difficulties with convergence. All the cases ran had less than 0.1% of the time steps that had to proceed to the next time step without converging after reaching the maximum of 100. For example from an analysis of the simulation log for EC08 (Fig. 20), it can be clearly seen that the cumulative plot is skewed towards the time steps converging with fewer than 20 iterations with only 0.7% of the time steps requiring more.

The plot beyond is not shown to prevent clutter though it is useful to note that eventually 0.6% of the time steps still did not manage to converge beyond 100 iterations. The median time steps require around 8.7 iterations for convergence, with an interquartile range of around 2 iterations. The results showed that even in real world simulations, the coupled motion solver with Aitkens dynamic under-relaxation did not have any problems with convergence most of the time. As such, it is clear that setting the maximum number of allowed iterations to 100 had been over-conservative for the current case, which was only chosen to check if convergence was possible with further iterations. From the results above, even setting the maximum to 20 is possible since it seems that most of the time steps that did not converge in 20 iterations would not converge in 100 iterations as well. However, a safer value of 50 is recommended for future runs since only rarely would that number of iterations would be required and will not drastically increase the total
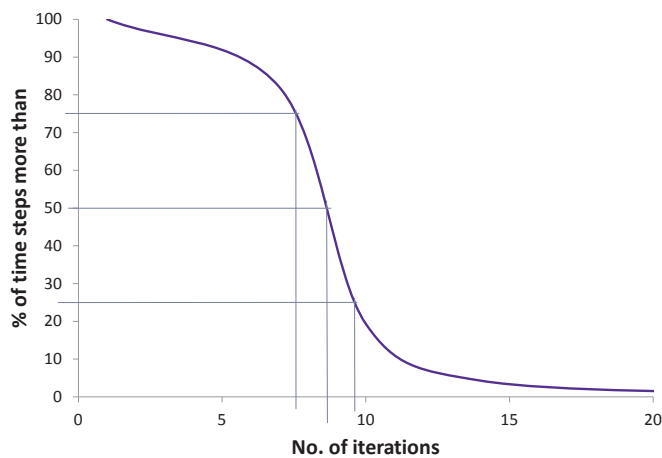
Fig. 20. Cumulative frequency plot of the time steps converging with more than a certain number of iterations (Regular waves of EC08, $\theta = 30°$).

simulation time.

4. Conclusions

From the experimental results obtained for the floating wind turbine setup on a tensioned leg platform (Laugesen and Hansen, 2015), a validation study was performed to test out the coupled 6-DoF rigid body motion solver implemented in Chow and Ng (2016). The developed solver was brought into test with an experimental floating wind turbine setup on a tensioned leg platform. Some of the unknown parameters were tuned with decay tests on the surge, pitch and yaw modes. With the finalised parameters, a very good match of the damping ratio and natural frequency was obtained. A modified restrain system was implemented to model the tendons with custom force-displacement functions and also apply zero force when the ropes are slack. The simulation of the floating system under regular and focused waves were ran and it has been shown with reasonable validations that the coupled 6-DoF rigid body motion solver was able to capture the wave loads on the floating wind turbine and determine its response. These wave impact forces produced from non-linear wave interaction also includes complex interactions between the restrain tendons and the floating structure. Beyond the current validation study, the simulations could be adapted to allow testing out of different setup configurations for design optimisation of the restrains and allowable maximum displacements, reducing the need to perform many different physical experiments in the wave basin.

4.1. Recommendations and future works

In the validation tests with experimental data, several problems were encountered. Firstly, the wave generation boundary conditions from the *ihFoam* libraries were not able to generate a good representation of less severe sea states (i.e. EC05). This may not be a problem in the current study due to the preferences for validating more severe sea states, running the cases with smaller wave heights and periods may however provide useful insight on specific cases. Secondly, the lack of a good representation of focused waves in the simulations comparable to the experiments has prevented comparison of the results for the cases. An alternative wave generation/absorption package *waves2foam* (Jacobsen et al., 2012) could be a good option for application to the current cases or reference to improve the present implementation.

References

Butterfield, S., Musial, W., Bonnie, R., 2006. Energy from offshore wind. In: Offshore Technology Conference.

Chow, J.H., Ng, E.Y.K., 2016. Strongly coupled partitioned six degree-of-freedom rigid body motion solver with Aitken's dynamic under-relaxation. Int. J. Naval Architect. Ocean Eng. 8, 320–329 Society of Naval Architects of Korea.

Deshpande, S., Anumolu L, S., Trujillo, M.F., 2012. Evaluating the performance of the two-phase flow solver interFoam. Comput. Sci. Discov. 5 (8), 320–329 Naval Architecture and Ocean Engineering.

Higuera, P., Lara, J.L., Losada, I.J., 2013a. Realistic wave generation and active wave absorption for Navier–Stokes models: application to OpenFOAM®. Coast Eng. 1 (71), 102–118.

Higuera, P., Lara, J.L., Losada, I.J., 2013b. Simulating coastal engineering processes with OpenFOAM®. Coast Eng. 1 (71), 119–134.

Inman, D.J., 2009. Engineering Vibrations. Pearson Education International.

Jacobsen, N.G., Fuhrman, D.R., Fredsøe, J., 2012. A wave generation toolbox for the open-source CFD library: OpenFoam®. Int. J. Numer. Methods Fluid. 70, 1073–1088.

Johannessen, K., Meling, T.S., Haver, S., 2002. Joint distribution for wind and waves in the Northern North sea. Int. J. Offshore Polar 12, 1–8 Mar.

Laugesen, R., Hansen, A.M., 2015. Experimental Study of the Dynamic Response of the DTU 10 MW Wind Turbine on a Tension Leg Platform. Technical University of Denmark.

Myhr, A., Bjerkseter, C., Agotnes, A., Nygaard, T.A., 2014. Levelised cost of energy for offshore floating wind turbines in a life cycle perspective. Renew. Energ. Jun. 66, 714–728.

Roland Berger, S.C., 2013. Offshore Wind toward 2020 - on the Pathway to Cost Competitiveness.